RSC Advances

PAPER

View Article Online
View Journal | View Issue

Cite this: *RSC Adv.*, 2023, **13**, 28198

Synergistic effect of a $Bi_2Zr_2O_7$ and hydroxyapatite composite: organic pollutant remediation, antibacterial and electrochemical sensing applications†

K. Pompapathi,[ab] K. S. Anantharaju,*[ac] B. S. Surendra,[c] S. Meena,[c] B. Uma,[c] Arpita Paul Chowdhury*[c] and H. C. Ananda Murthy *[de]

Global concern regarding the energy crisis and environmental pollution is increasing. The fabrication of efficient catalysts remains a long-term goal. Recently, green synthesis methods for catalyst fabrication have attracted the scientific community. Herein, a simple approach to synthesize bismuth zirconate-hydroxyapatite (BZO-HA) nanocomposites using *Mentha spicata* (mint) leaves as a reducing agent *via* a combustion method has been reported. The use of a green reducing agent provided economic attributes to this work. Among the prepared samples, the BZO-HA (20%) composite exhibited superior photocatalytic activity. The photodegradation efficiency of the composite reached 90.3% and 98.4% for methylene blue (MB) and rose Bengal (RB) dyes, respectively. The results showed the excellent optical performance of the prepared composites. The constructed sensor (BZO-HA 20%) for the very first time showed outstanding selectivity and performance towards sensing lead nitrate and dextrose compared to bare bismuth zirconate (BZO) and hydroxyapatite (HA). A three-electrode system using 0.1 M KCl was used for the study. The synthesized composite BZO-HA (20%) can sense lead nitrate and dextrose over the concentration range of 1–5 mM in the potential range from −1.0 V to +1.0 V. The BZO-HA composite was also investigated against Gram-negative (*S. typhi*) and Gram-positive (*S. aureus*) bacteria for antibacterial activity studies. Enhanced antibacterial activity was observed compared to bare BZO and HA catalysts. Thus, the prepared BZO-HA nanocomposite exhibited multifunctional applications.

Received 2nd August 2023
Accepted 8th September 2023

DOI: 10.1039/d3ra05222b

rsc.li/rsc-advances

1 Introduction

Recently, energy shortages, and environmental pollution have become major concerns for sustainable environmental development. The research community is fascinated by the unique properties of nanomaterials. Hence, there has been a rapid increase in the synthesis of nanomaterials and their applications in electronics, environmental remediation, medicine, clothing, pesticides, and fertilizers are being explored.[1] Water streams from industrial waste containing organic dyes, pharmaceutical compounds, and pesticides are considered an environmental hazard.[2] The organic solutions, especially dyes, affect the aquatic environment due to reduced penetration of light in the water stream. Among the industrial dyes, rose bengal (anionic dye) and methylene blue (cationic dye) are carcinogenic organic molecules used in various industries.[3,4] So far, various nanomaterials have been explored for potential application.

Bismuth-based oxides with formula $A_2B_2O_7$ belong to the pyrochlore structural family and have shown potentiality for photocatalytic reactions under visible light. The crystal has a cubic lattice with an $Fd\bar{3}m$ space group and $\bar{3}m$ symmetry. The 'A' cations are eight-coordinated and the 'B' cations are six-coordinated occupying 16d and 16c sites. The 48f sites are occupied by oxygen ions with 2 mm symmetry and can respond to visible light.[5,6] The pyrochlore structure is shown in Fig. 1.

The scientific community worldwide has synthesized $Bi_2Zr_2O_7$ photocatalysts by various routes. Wu *et al.* synthesized $Bi_2Zr_2O_7$ by a facile sedimentation–calcination method and

[a]*Dr. D. Premachandra Sagar Centre for Advanced Materials, Dayananda Sagar College of Engineering, Shavige Malleshwara Hills, Kumaraswamy Layout, Bengaluru 560111, India. E-mail: iamananth4477@gmail.com*

[b]*Department of Material Science, Mangalore University, Mangalagangotri, Mangalore 574199, Karnataka, India*

[c]*Department of Chemistry, Dayananda Sagar College of Engineering, Shavige Malleshwara Hills, Kumaraswamy Layout, Bengaluru 560111, India. E-mail: chemarpitachowdhury@gmail.com*

[d]*Department of Applied Chemistry, School of Applied Natural Science, Adama Science and Technology University, Adama, P O Box 1888, Ethiopia. E-mail: anandkps350@gmail.com*

[e]*Department of Prosthodontics, Saveetha Dental College & Hospital, Saveetha Institute of Medical and Technical Science (SIMATS), Saveetha University, Chennai 600077, Tamil Nadu, India*

† Electronic supplementary information (ESI) available. See DOI: https://doi.org/10.1039/d3ra05222b

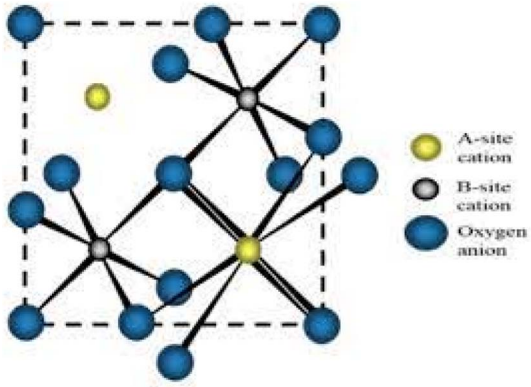

Fig. 1 Pictorial representation of pyrochlore structure (reproduced with permission from ref. 6. Copyright ACS 2019).

showed the degradation of methyl orange (MO).[7] Liu *et al.* prepared $Bi_2Zr_2O_7$ by sol–gel method using citric acid and applied it for the photodegradation of tetracycline.[8] Luo *et al.* reported the coprecipitation method of synthesis of $Bi_2Zr_2O_7$ photocatalyst for Cr(VI) reduction.[9] Rajashekharaiah *et al.* synthesized Dy^{3+}-doped $Bi_2Zr_2O_7$ by hydrothermal route for antibacterial and anti-cancer applications.[10]

Materials at the nano level have enhanced antibacterial activity. Nanomaterials interact with bacterial cell membranes due to the surface-to-volume ratio of nanomaterials.[11] Silver nanoparticles (Ag NPs) have been effectively utilized as antibacterial agents, however, the application of Ag ions is restricted due to their high cytotoxicity and release rate.[12] For this reason, there is continuous research on alternative approaches and in this regard, bismuth zirconate is a good choice.

Currently, the consumption of toxic heavy metals by humans is high, either directly or indirectly through food, water, and skin.[13] The detection of trace heavy metals is usually achieved through various spectroscopic techniques, where the most commonly used are X-ray fluorescence (XRF) and neutron activation analysis (NAA). X-ray fluorescence (XRF) is a rapid, non-destructive screening method for samples containing high concentrations of major elements. However, it has poor detection limits for most trace elements.[14] Neutron activation analysis (NAA) is a non-destructive method and it is used as a reference method to test the accuracy of other analytical methods.[15] This method is based on the conversion of stable isotopes of chemical elements to unstable radioactive isotopes by irradiation with thermal neutrons within a nuclear reactor.[16] Thus elements having abundant isotopes with a high cross-section for thermal neutrons are of interest. On the contrary, NAA has extremely low sensitivity for lead.[17] Nowadays electrochemistry represents an interesting alternative technique. The fabricated electrochemical devices are of low cost, have minimal sample preparation requirements, and have simple, user-friendly operation procedures. Thus, contamination by reagents or losses by adsorption on containers is drastically decreased. Thus, due to the advantages of electrochemical devices, metal oxide-based semiconductors are extensively employed in sensing techniques. $Bi_2Zr_2O_7$ is a potential candidate but for practical applications the high recombination rate of photogenerated e^-–h^+ pairs restricts its broader application.[18] Thus, the synthesis of heterostructured photocatalysts, with characteristics of high e^-–h^+ separation efficiency has recently caught great attention.[19] To date, numerous catalysts have been reported for decontamination and water splitting. Nevertheless, photoactivity in the visible region is limited due to the wide band gap, making them inefficient for solar light applications. Thus, the continuous development of novel heterojunction visible-light-driven (VLD) photocatalysts is a challenge.[20]

In this framework, ceramic-based biomaterial hydroxyapatite (HA) has earned the utmost importance and shows a resemblance to the human skeleton and tooth enamel.[21] Owing to the excellent biocompatible properties of HA, it is widely used in chemistry, biology, and medicinal fields and its derived products have received wide attention.[22] A few works were reported in the literature where HA is coupled to form a composite for the photocatalytic degradation of dyes, for instance a-Fe_2O_3-HAp,[23] CS/HA,[24] CS/HA/Fe_3O_4,[25] HA/gold,[26] and HA/Fe_3O_4 NPs.[27]

Heterostructure composites of $Bi_2Zr_2O_7$ have been far less explored for various applications; a very limited body of literature is available for the coupling of $Bi_2Zr_2O_7$ with other semiconductors. Qu *et al.* synthesized $Bi_2Zr_2O_7$/g-C_3N_4/Ag_3PO_4, a dual Z-scheme photocatalyst, *via* the facile coprecipitation method.[18] Herein, for the first time, *Mentha spicata* was applied as a stabilizing agent to prepare the composite. In this study, $Bi_2Zr_2O_7$-hydroxyapatite (BZO-HA) composites with 10, 20, and 30 wt% HA were synthesized by the solution combustion method for the sensing of dextrose and Pb^{2+}, as well as for antibacterial and photocatalytic study. The synthesized BZO-HA nanocomposite was characterized by X-ray diffraction (XRD), scanning electron microscopy (SEM), Fourier-transform infrared spectroscopy (FT-IR), electrochemical impedance spectroscopy (EIS), and UV-visible spectroscopy (UV-vis DRS). The present work provides a good example for the modification of BZO-based materials for efficient catalytic activity.

2 Experimental

2.1 Materials

Bismuth nitrate pentahydrate ($Bi(NO_3)_3 \cdot 5H_2O$, 98%) and zirconyl(IV) nitrate hydrate [$ZrO(NO_3)_2 \cdot H_2O$, 99%], were procured from Sigma-Aldrich Chemicals, India. Isopropyl alcohol (IPA, 99%) and ammonium oxalate (AO, 99%) were obtained from Merck, India. Ascorbic acid (AA, 99%), methylene blue (MB, 82%), rose Bengal (RB, 85%), lead(II) nitrate ($Pb(NO_3)_2$, 99%), potassium chloride (KCl, 99%), and dextrose were purchased from Loba chemical company. Analytical (AR) grade reagents and distilled water were used throughout the reactions.

2.2 Synthesis

2.2.1 Preparation of *Mentha spicata* (mint) extract. Freshly picked *Mentha spicata* leaves (2 g) were collected and washed

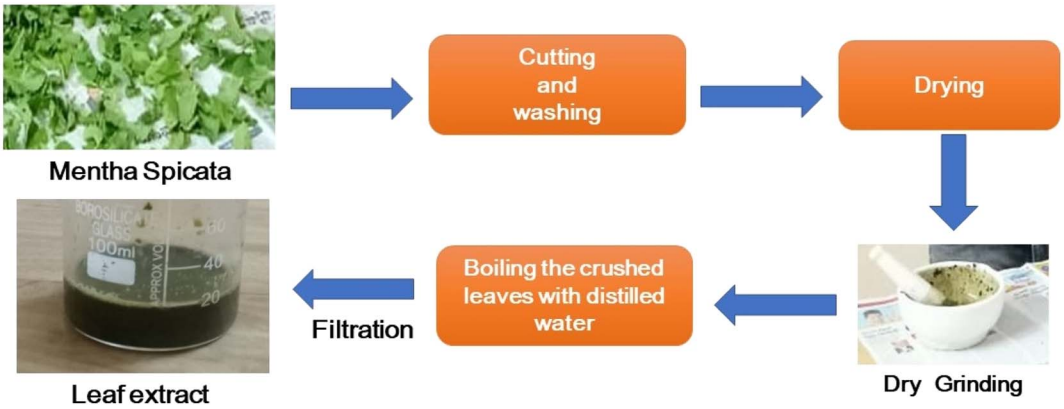

Fig. 2 Pictorial representation of preparation of *Mentha spicata* leaf extract.

with distilled water, followed by drying. The leaves were then crushed using a mortar and pestle. The crushed leaves were boiled with 30 mL of water for 30 min. After cooling, the mixture was filtered using filter paper (Whatman No. 1). The obtained green-colored extract was used as a reducing and stabilizing agent (Fig. 2).

2.2.2 Preparation of $Bi_2Zr_2O_7$ (BZO) nanoparticles. In order to prepare the BZO NPs by combustion method, zirconyl(IV) nitrate hydrate (1.947 g) was combined with bismuth nitrate pentahydrate (3.326 g) as an oxidizer and mint extract (10 mL) as fuel. These starting materials were thoroughly mixed in a porcelain crucible to obtain a homogeneous mixture and then inserted into a preheated muffle furnace (500 °C). Finally, yellow-colored BZO nanoparticles were obtained.

2.2.3 Preparation of hydroxyapatite (HA). For the preparation of hydroxyapatite, the synthesis method reported by Acharya *et al.*[28] was adopted. Silver carp fish waste was used as a raw material. The bone samples were separated and cleaned thoroughly with distilled water to remove unwanted particles and the sterilized in a hot air oven for 1 h at 80 °C. The bones were later crushed and placed in a ceramic crucible in a muffle furnace at 900 °C for 3 h to obtain hydroxyapatite crystals.

2.2.4 Preparation of the BZO-HA composite. The BZO-HA composite was prepared using the solution combustion method. Typically, $Bi(NO_3)_3 \cdot 6H_2O$ (2.5 g), $ZrO(NO_3)_2$. H_2O (1.46 g) and mint extract (6 mL) were homogeneously mixed in a crucible. Then the prepared HA sample (at 10 wt%, 0.25 g) was added to the precursor mixture and placed in a furnace at 500 °C for 10 min to obtain the BZO-HA (10%) composite. Similarly, the other compositions with HA at 20% (0.5 g) and 30% (0.75 g) were prepared and the samples are labelled as BZO-HA (10%), BZO-HA (20%), and BZO-HA (30%), respectively.

2.3 Characterization

X-ray diffraction patterns of the phase structures of the prepared samples were examined using a Bruker X-ray powder diffractometer with CuKα radiation and $\lambda = 1.54187$ Å in the range of 20–80°. Fourier-transform infrared spectroscopy (FTIR) was applied for functional group detection using a Thermo Fischer Scientific instrument. Field-emission scanning electron microscopy (FE-SEM) was carried out using a Model Mira3 - XMU, TESCAN. UV-Vis diffuse reflectance spectroscopy (UV-vis DRS) was used to analyze the optical absorption properties of the samples (Lambda 365 UV-visible Spectrophotometer). An electrochemical analyzer (CHI 608E potentiostat) was used to perform the electrochemical studies.

2.4 Antibacterial testing

The synthesized sample BZO-HA (20%) with the best morphology, crystallinity, shape and size from XRD and SEM analysis was selected for the antibacterial test using the well diffusion method. *S. typhi* and *S. aureus* inoculums measuring 200 μL each, were evenly distributed using a plate spreader on sterilized agar plates. Each plate was prepared with five 0.6 cm-diameter wells using a borer. The wells were filled with 50 μL of sample containing 100 μg, 200 μg, 300 μg, and 400 μg. The middle well was filled with 50 μL of DMSO as a negative control. The bacterial plates were kept at 37 °C during incubation for 24 h and the zone of inhibition was measured in mm.

2.5 Photocatalytic experiments

The catalytic experiments was conducted under the direct sunlight irradiation on a sunny day in the month of May in the DSCE college campus, Bangalore from 11:00 am to 1:00 pm. In this study, the prepared catalyst (100 mg) was dispersed in 250 mL of 20 ppm methylene blue dye solution. Then to ensure adsorption–desorption equilibrium between the catalyst and MB dye, the solution was constantly stirred for a period of 15 min in the dark. At regular time intervals, 5 mL of suspension is taken and the absorbance of the supernatant solution is recorded in a UV-vis spectrophotometer at 664 nm. Based on the Beer–Lambert law,[29] the percentage degradation of the dye was determined using eqn (1):

$$\% \text{ of degradation} = (C_0 - C_t)C_0 \times 100\% \quad (1)$$

where the absorbance of the dye at the initial stage and at time "t" is denoted C_0 and C_t, respectively. A similar process was adopted for RB dye and absorbance of the supernatant solution was recorded at 540 nm.

2.6 Electrochemical measurements

The electrodes were prepared by mixing the synthesized samples, graphite, and silicon oil in a ratio of 1 : 3 : 1 to obtain a paste. The paste was filled in a Teflon tube and the Teflon tube was smoothed over wax paper. A copper wire was used for the electrical contact with the three-electrode system for the electrochemical measurements.[30]

3 Results and discussion

3.1 Characterization of samples

3.1.1 XRD analysis. The XRD patterns confirmed the phase structure and crystallinity of the prepared samples (Fig. 3). The $Bi_2Zr_2O_7$ (BZO) exhibited sharp diffraction peaks at 27.7°, 28.5°, 31.1°, 33.25°, 44.3°, 47.5°, 51.2°, 55.5°, and 56.9° which correspond to the (220), (222), (044), (400), (333), (404) (620), (226) and (444) reflections, respectively. The diffraction planes were in good agreement with the reported literature.[31–33] The intense and strong diffraction peaks of BZO confirmed the high crystallinity of the sample. The characteristics diffraction peaks obtained for pure hydroxyapatite (HA) were amorphous in nature and the peaks at 2 theta values of 25.8°, 31.73°, 32.3°, 39.7°, 46.6°, 49.5°, 51.4°, 53.2°, and 58.1° are well indexed to the (002), (211), (112), (310), (222), (213), (410), (004), and (501) planes, respectively, of the hexagonal phase with $P6_3/mmc$ (176) space group and are in accordance with the standard JCPDS card No. 09-0432. It was found that on coupling HA with BZO (Fig. 3d and e), diffraction peaks for HA appeared at 25.8°, 31.7°, 46.6°, 39.7°, and 53.4°. For BZO-HA (20%) and BZO-HA (30%), no peaks of other phases were observed. However, in the XRD pattern for BZO-HA (10%), impurity peaks of the ZrO_2 phase were observed at 24.8°, 29.8°, and 49.6°, which are indicated by # in the XRD pattern. On further increasing the concentration of HA in the composite, the impurity peaks disappeared slowly and also no peak shift was observed in the composite. Thus, the coexistence of HA peaks in BZO confirmed the formation of a composite.

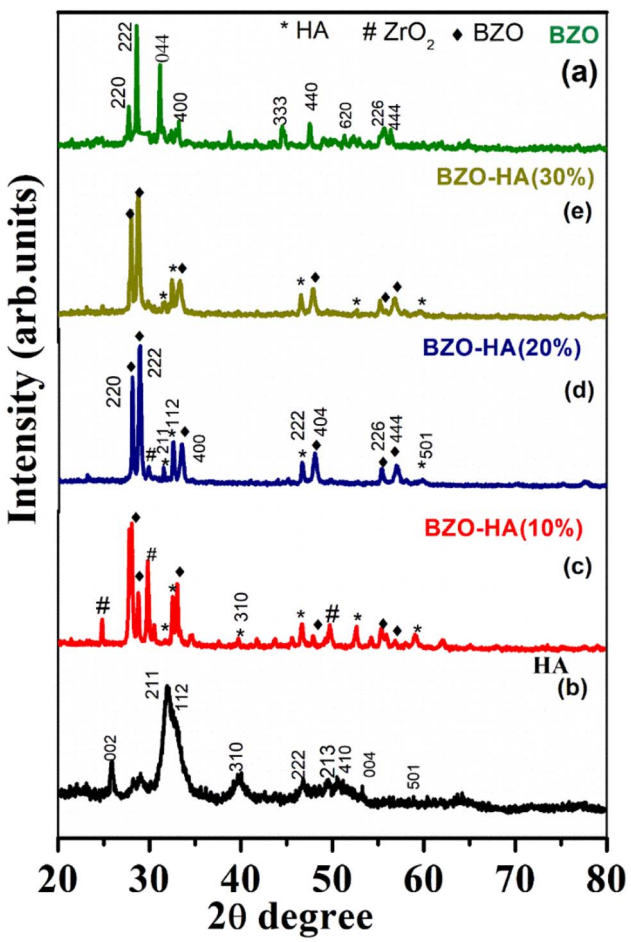

Fig. 3 XRD patterns of the prepared samples: BZO (a), HA (b), BZO-HA (10%), BZO-HA (20%) and BZO-HA (30%) (c–e).

The crystallite sizes of the BZO, HA, and composites were calculated by means of the Debye–Scherrer equation. The crystallite sizes for BZO, HA, BZO-HA (10%), BZO-HA (20%), and BZO-HA (30%) were deduced to be 13.71 nm, 19.72 nm, 16.11 nm, 25.29 nm, and 23.55 nm respectively. Thus, XRD results revealed that the obtained samples are of high crystallinity.

3.1.2 SEM analysis. The micro-surface morphology of the prepared catalyst was characterized by the SEM analysis. Typical SEM images of $Bi_2Zr_2O_7$ (BZO), hydroxyapatite (HA), and the composites (BZO-HA) are displayed in Fig. 4. As shown in the Fig. 4a, BZO consists of smooth and irregular triangular plates while HA showed ultrathin nanoflakes with partial folds on the surface (Fig. 4b). However, on forming the composite BZO-HA (10%), it was observed that HA particles are distributed on the surface of the BZO, leading to the formation of a heterostructure. With increasing concentration of HA (20% and 30%) a hierarchical cluster structure formation was witnessed (Fig. 4c–e).

3.1.3 UV-vis diffuse reflectance spectroscopy. The optical properties of BZO, HA and the composite samples are illustrated in Fig. 5. The spectra of the composites displayed intense light absorption in the region of 500–550 nm. The optical absorption edge is extended to around 475 nm for the BZO particles. However, low light absorption ability was observed for the HA, which might be due to the light scattering effect.[34] The reflection in the visible range was imperfect for HA and a small absorption in this range is observed. The experimental band gaps for BZO and BZO composites were calculated from the Tauc plots using the Kubelka–Munk equation, $F(R) = (1 - R)^2/2R$,[35] where R is the total diffuse reflectance of the representative samples and $F(R)$ is the ratio of the absorption and scattering coefficients of the samples.

The E_g values of 2.26, 3.61 2.67, 2.79, and 2.86 eV for BZO, HA, BZO-HA (10%), BZO-HA (20%), and BZO-HA (30%), respectively, were obtained from the intercept of the tangent to the absorption curves and are listed in Table 2. The calculated band gap of HA is consistent with the reported literature indicating the presence of oxygen vacancies in the phosphate group.[36,37] The band gap of the BZO-HA composites increased upon incorporation of HA, which might be due to the interaction between the chemical constituents of HA and BZO.

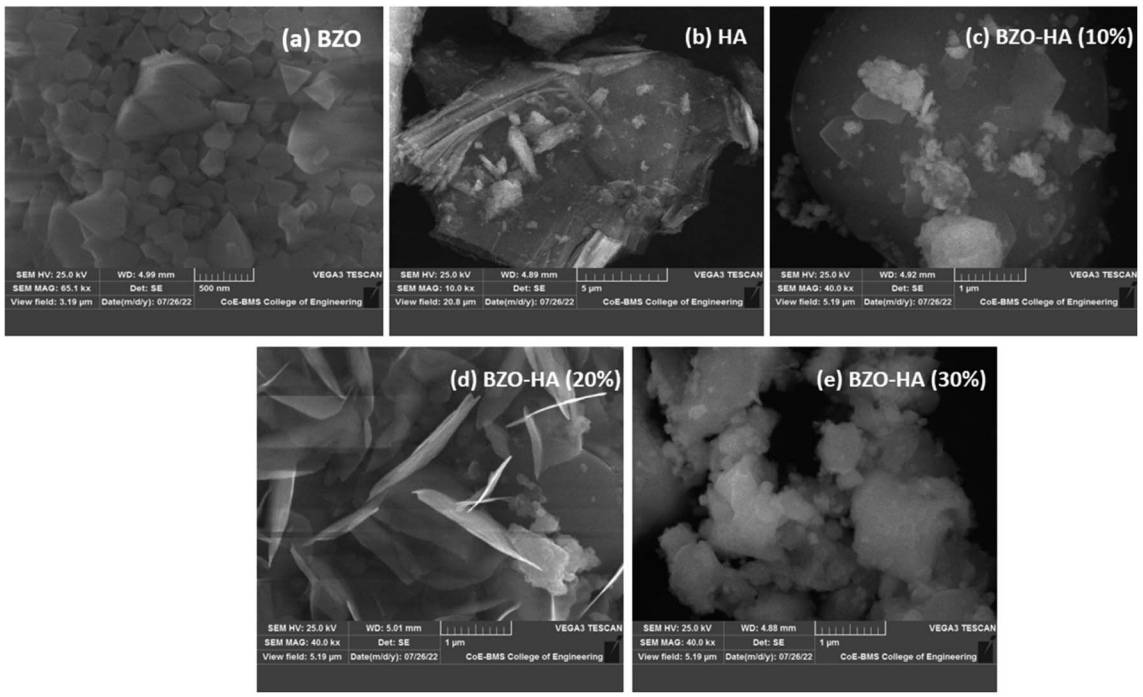

Fig. 4 FESEM images of (a) BZO, (b) HA, and (c–e) BZO-HA composite with different concentrations of HA.

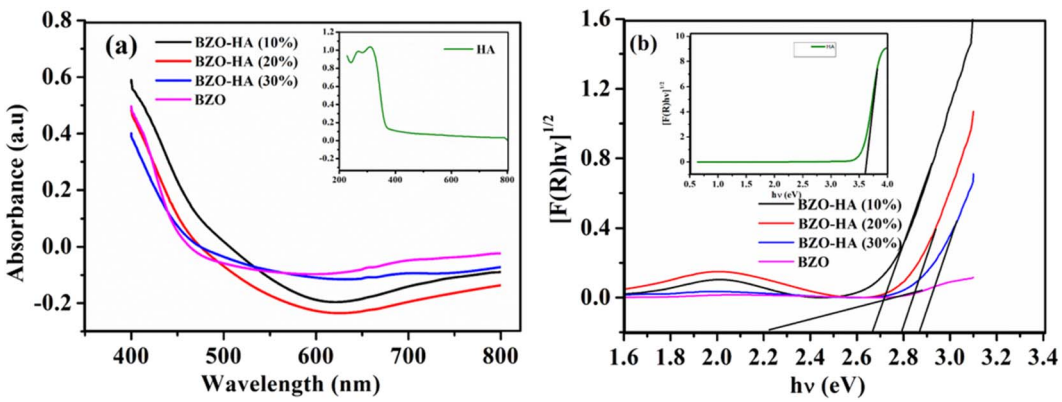

Fig. 5 (a) UV-vis diffuse reflectance spectra (DRS) and (b) band gap *versus* photon energy plots of the as-synthesized BZO, HA and BZO-HA composites.

Furthermore, the optical phonon energy of the composites was enhanced compared to that of bare BZO, which can be assigned to the Burstein–Moss effect. Similar results were reported by Guo *et al.*[38] Thus the catalytic performance not only depends on the light absorption phenomenon but on other factors, as reported in the previous literature.[39]

3.1.4 FTIR analysis. The FTIR spectra for the BZO, HA and the composites of BZO with HA are shown in Fig. 6. The peak observed at 820 cm^{-1} is due to the NO_3^- group present in the BZO material. The peak around 1250 cm^{-1} is due to carbonyl double bonded (C=C) carbons of aromatic compounds present in *Mentha spicata* leaf extract. In the spectra for HA and the composites of HA with BZO, the peak around 870 cm^{-1} was found to be due to $\nu_2(CO_3)^{2-}$ stretching, the region at 1350–1470 cm^{-1} belongs to $\nu_3(CO_3)^{2-}$.[40] The ν_3 and ν_4 bands around 1260 cm^{-1} and 650 cm^{-1} are from PO_4^{2-} and PO_4 groups, respectively. The broad band found at 2500 cm^{-1} corresponds to the C–H stretching of the aromatic ring. The band at 3750 cm^{-1} indicates the OH group stretching vibrations.[41]

3.1.5 Electrochemical studies. Cyclic voltammetry (CV) and electrochemical impedance spectroscopy (EIS) were employed to study the electrochemical features of the as-synthesized HA and BZO-HA nanocomposites. The CV measurements were performed using the conventional three-electrode setup in aqueous 0.1 M KCl as the electrolyte. Fig. 7a–d display the CV curves in the range of potentials between +1.0 and −1.0 V for HA and BZO-HA (10%, 20% and 30%) nanocomposite-modified graphite electrodes with varying scan rate from 0.01 to 0.05 V

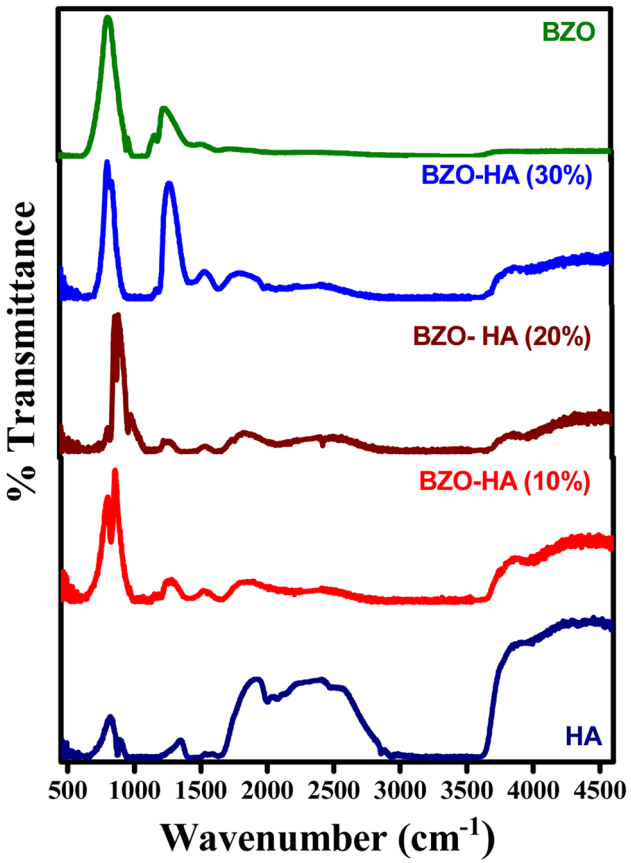

Fig. 6 FTIR spectra of BZO, HA and BZO-HA composites.

s^{-1}. The presence of redox peaks confirmed the pseudocapacitance behaviour of the electrodes.[42–44]

The specific capacitance (SPcv) was evaluated from the CV plots using eqn (2), as depicted in Table 1.

Table 1 Specific capacitance calculated from CV curves at various scan rates

Specific capacitance ($\times 10^{-2}$ F g^{-1})				
Scan rate	BZO-HA (10%)	BZO-HA (20%)	BZO-HA (30%)	HA
0.01	19.9	13.5	10.7	6.7
0.02	15.3	8.0	9.2	4.3
0.03	13.1	6.2	7.2	4.0
0.04	10	5.1	6.6	3.6
0.05	9.2	4.2	5.7	3.3

$$SP_{CV} = \frac{\int I dV}{v \times m \times \Delta V} \quad (2)$$

It is clear from Table 1 that the BZO-HA (10%)-modified graphite electrode exhibited the highest specific capacitance with high exposure area as compared to other electrodes. This observation revealed that the BZO-HA (10%) modified graphite electrode has excellent electrochemical behaviour. The stability of the nanomaterial was confirmed by CV at different scan rates (0.01 mV s^{-1}–0.05 mV s^{-1}) for the BZO-HA (10%)-modified graphite electrode, as depicted in Fig. 7a. It was predicted that the shift in the cathodic and anodic peak areas of CV curves when the scan rate was increased from 0.01 mV s^{-1} to 0.05 mV s^{-1} due to an internal resistance over the electrode surface.[45–48] All the CV curves retained their redox peaks at different scan rates, confirming the pseudocapacitance behaviour of the nanomaterial. As can be seen in Table 1, there is a decreasing trend in SPcv values with increasing scan rates owing to a comparatively insufficient faradaic redox process at higher scan rates.[45,49]

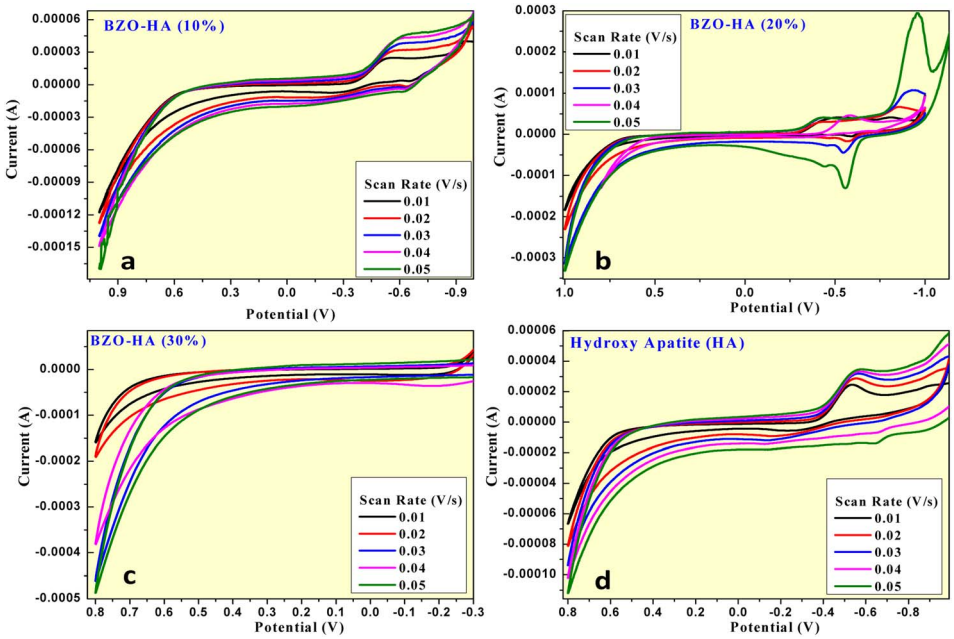

Fig. 7 CV curves at various scan rates for HA and the BZO-HA (10%, 20% and 30%) nanocomposites (a–d).

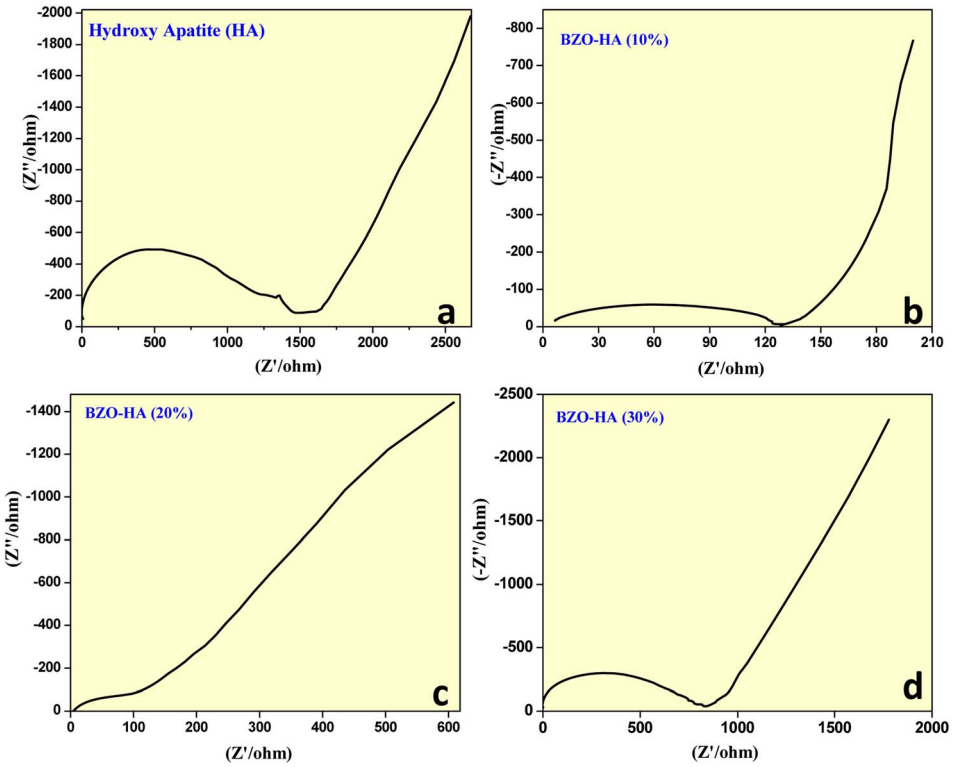

Fig. 8 Nyquist plots for HA and BZO-HA (10%, 20% and 30%) nanocomposites at various scan rates.

Fig. 8a–d show the EIS spectra of HA and the BZO-HA (10%, 20% and 30%) nanocomposite-modified graphite electrodes. The high-frequency regions displayed by the respective electrodes comprise a semicircle while a straight line was displayed for the lower frequency regions. Using the diameter of the semicircle, the charge transfer resistance (R_{ct}) values of the electrode and electrolyte interface can be obtained. The calculated R_{ct} values of the HA and BZO-HA (10%, 20%, 30%) nanocomposite-modified graphite electrodes were found to be 1500 Ω, 120 Ω, 100 Ω and 900 Ω, respectively. There was a slight appearance of a semicircle for BZO-HA (20%). The slope from the straight line in the low-frequency region for BZO-HA (10%) tended slightly towards 90° as compared to the other modified electrodes, which confirms the capacitive nature. The BZO-HA

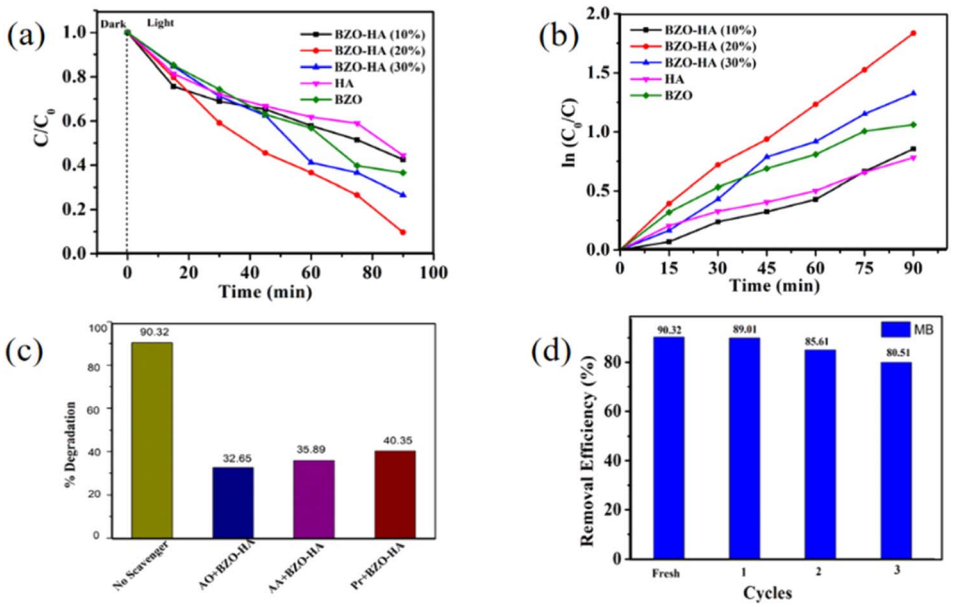

Fig. 9 (a) Plot of (C/C_0) *vs.* irradiation time for the pure BZO, HA and BZO-HA composites. (b) ln plot of (C_0/C) *vs.* irradiation time. (c) Effects of scavengers on MB dye degradation. (d) Reusability.

(20%) nanocomposite-modified electrode exhibited a low R_{ct} value, which revealed that the material can be utilized as a semiconducting material for enhancing photocatalytic applications.[50–52]

3.2 Photocatalytic evaluation of the BZO, HA and BZO-HA composites

To evaluate the photocatalytic properties, a series of experiments were carried out with the BZO-HA composites under visible light irradiation. The degradation profiles for MB and RB are presented in Fig. S1 and S2.† The characteristic absorbance peaks of MB and RB at wavelengths of 664 nm and 540 nm, respectively, gradually decreased within the 90 min irradiation time. It is clear from the obtained absorbance plot that the BZO-HA (20%) composite could effectively decompose the dyes compared to bare BZO and HA. The photocatalytic activity performance is enhanced compared to that BZO because the recombination of electron and hole pairs decreases due to the greater charge separation in the composites. Fig. 9a and 10a present the MB and RB degradation efficiency of the different photocatalysts over time.

The degradation efficiency for MB was found to be in the sequence BZO-HA (20%) > BZO-HA (30%) > BZO > BZO-HA (10%) > HA while the degradation efficiency for RB follows the order BZO-HA (20%) > BZO-HA (30%) > BZO-HA (10%)> BZO > HA. The removal efficiencies of MB and RB with BZO-HA (20%) were found to be 90.32% and 98.44%, respectively. To better understand the photocatalytic efficiency, a pseudo-first-order model was established for the experimental data to obtain the kinetic results. The plots of ln C_0/C as a function of time for BZO, HA, and BZO-HA composites are shown in Fig. 9b and 10b. The rate constants for BZO-HA (20%) for MB and RB dye were estimated to be 0.020 min^{-1} and 0.04 min^{-1}, respectively. The percentage degradation efficiencies and rate constants for pure BZO, HA, and the nanocomposites for MB and RB dye are summarized in Table 2. The superior performance by the composite BZO-HA (20%) is possibly due to the aggregated morphology and the synergistic effect between BZO and HA, which further hinders photogenerated electron and hole recombination. Thus, the MB and RB dye degradation efficiency with the composite photocatalyst was improved markedly compared to the bare catalyst. For comparison, other reported catalysts for the degradation of RB and MB dye are shown in Table 3.

To analyze the active radical responsible for the photocatalytic degradation mechanism, radical-trapping experiments were performed. The scavengers ammonium oxalate (AO), ascorbic acid (AA), and isopropanol (Pr) were employed to trap photogenerated holes, superoxide anion ($O_2^{\bullet -}$) and hydroxyl radicals ($OH^{\bullet}$), respectively.[53] The degradation efficiency for MB dye with BZO-HA (20%) composite decreased to 35.4%, 40.82%, and 49.62% while for RB dye the degradation efficiency is only 32.65%, 35.89% and 40.35% with the addition of AO, AA, and Pr, respectively (Fig. 9c and 10c). This data reveals that all three radicals actively participated in the catalytic mechanism. From a practical application view, repeated cycles of MB and RB removal were carried out with BZO-HA (20%). After each cycle, the catalyst was centrifuged and washed with deionized water. A slight decrease in the degradation efficiency was observed from the 1st to the 3rd cycle. The catalyst showed good degradation efficiency (80.5% and 87.9%, respectively) for MB and RB dye even after the 3rd repeated cycle (Fig. 9d and 10d).

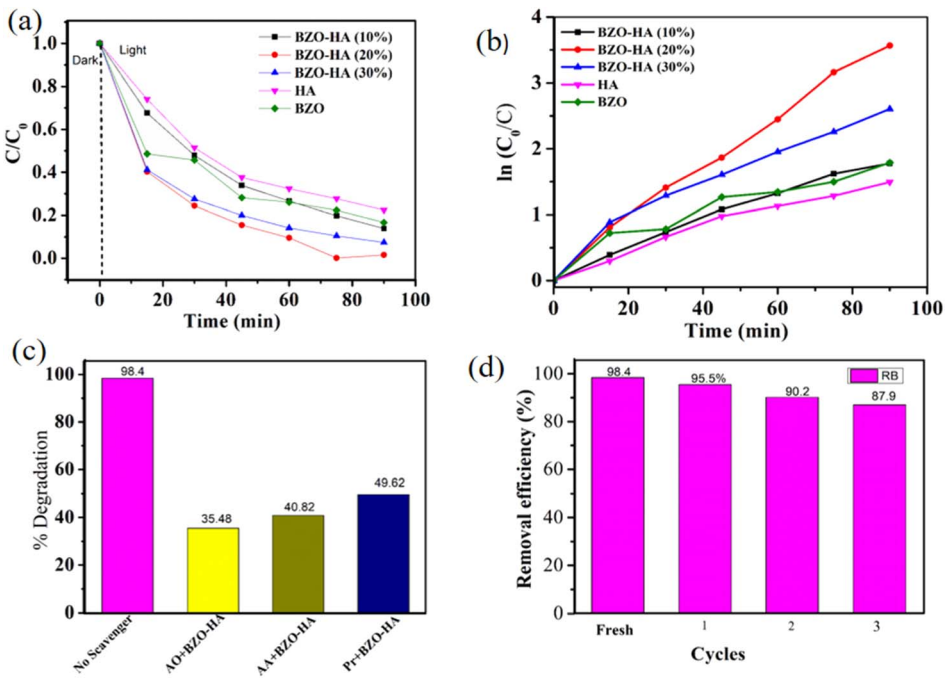

Fig. 10 (a) Plot of (C/C_0) *vs.* irradiation time over pure BZO, HA and the BZO-HA composites. (b) ln plot of (C_0/C) *vs.* irradiation time. (c) Effects of scavengers on RB dye degradation. (d) Resuablity.

Table 2 Degradation efficiency, kinetic data, calculated valence band (VB) and conduction band (CB) edge potentials for BZO and HA, and band gap energy (eV) of BZO, HA and BZO-HA composites

Photocatalyst	Degradation efficiency (%)		K (min^{-1})		Conduction band potential (CB) (eV)	Valence band potential (VB) (eV)	Band gap energy (E_g)
	MB	RB	MB	RB			
BZO	65.4	83.3	0.013	0.022	0.43	2.69	2.26
HA	55.6	77.5	0.009	0.017	−0.415	3.19	3.61
BZO-HA (10%)	57.4	86.1	0.008	0.021			2.67
BZO-HA (20%)	90.3	98.4	0.020	0.041			2.79
BZO-HA (30%)	73.5	92.6	0.015	0.031			2.86

Table 3 Comparison of the degradation efficiency of previously reported photocatalysts for MB and RB dyes

Sample	Dye	Concentration	Degradation efficiency (%)	Time	Ref.
$BaTiO_3$/GO	MB	5 mg L^{-1}	95	3 h	57
g-C_3N_4/ZnO	MB	10 ppm	90	120 min	58
SnO_2/TiO_2	MB	5 ppm	95	25 min	59
Ag/CeO_2/graphene	MB	20 mg L^{-1}	75	120 min	60
Sn-doped CeO_2–Fe_2O_3	MB	10 mg L^{-1}	94.6	2 h	61
CuO–Pb_2O_3	RB	—	99	90 min	62
α-Fe_2O_3@CeO_2	RB	5 ppm	93	75 min	63
Ag/CeO_2	RB	0.2 g L^{-1}	96	3 h	64
WO_2/α-$ZnMoO_4$	RB	1 μM	96	180 min	65
Sm-doped CeO_2	RB	5 ppm	90	90 min	66
Fe–NiO	RB	5 ppm	86	60 min	67
	MB	5 ppm	85	60 min	
BZO-HA (20%)	RB	20 ppm	98.4	90 min	Present work
	MB	20 ppm	90.3	90 min	

3.2.1 Proposed photocatalytic mechanism. For the efficient generation and separation of electron–hole pairs, the proper band structure of the photocatalyst is very essential. The band potentials can be theoretically predicted using empirical eqn (3) and (4):[31]

$$E_{VB} = X - E_e + 0.5E_g \quad (3)$$

$$E_{CB} = E_{VB} - E_g \quad (4)$$

where E_{VB} is the valence band edge potential, X is the electronegativity of the semiconductor, E_e is free electrons on the hydrogen scale (~4.5 eV)), and E_g is the band gap energy of the photocatalyst. The electronegativities of BZO and HA were found to be 6.06 and 5.89 eV respectively.[31,54] The VB and CB values of the BZO and HA samples based on the experimental results were found to be 2.69, 3.19 eV, and 0.43, −0.415 eV, respectively. Thus the CB and VB potentials of BZO and HA are at appropriate positions for the construction of a heterojunction. The photocatalytic mechanism scheme is presented in Fig. 11. According to the literature, both HA and BZO can generate electrons and holes under visible light. The CB edge potential of HA (−0.415 eV) is negative and lower than that of BZO (0.43 eV), and the VB potential of HA (3.19 eV) is more positive than that of BZO (2.69 eV). The photogenerated electrons on the surface of the HA easily migrate to the CB of the BZO while the holes present in the VB of the HA move to the VB of the BZO. Therefore, a type I heterojunction is effectively formed and this phenomenon reduced the recombination of photogenerated electron–hole pairs. For BZO-HA (20%), the CB potential (−0.415 *vs.* NHE) of HA is more negative than the standard redox potential of O_2/O_2^- (−0.33 eV chem *vs.* NHE, pH 7).[55] So, free electrons on the surface of HA react with the adsorbed oxygen molecule producing $^{\bullet}O_2^-$ species. Furthermore, the standard VB potentials of BZO and HA (2.69 and 3.19 eV) are more positive than the redox potential of $^{\bullet}OH/OH^-$ (+1.99 eV *vs.* NHE) and $^{\bullet}OH/H_2O$ (+2.27 eV *vs.* NHE).[56] It can be concluded that the h^+ can react with OH^- and H_2O to give rise to $^{\bullet}OH$ radicals. The results from the radical scavenger experiments also proved that holes, superoxide, and hydroxyl radicals were responsible for the degradation of the dye. Thus, the BZO-HA (20%) composite showed efficient photocatalytic activity compared to the single components.

3.3 Sensor studies of graphite-BZO-HA composite electrode

The prepared graphite-BZO-HA (10–30%) electrodes were extended toward sensor applications by electrochemical characterization. In the sensor examinations, we utilized prepared electrodes for sensing dextrose and lead metal in 0.1 M KCl electrolyte. The CV analysis of the prepared graphite-HA bare electrode was examined in the potential range of −0.8 V to +1.0 V, which confirmed little or no sensing ability for dextrose and lead nitrate (concentration 1–5 mM) (Fig. 12a and b). However, the prepared composite nanomaterials with different percentages of HA showed excellent sensing properties for lead

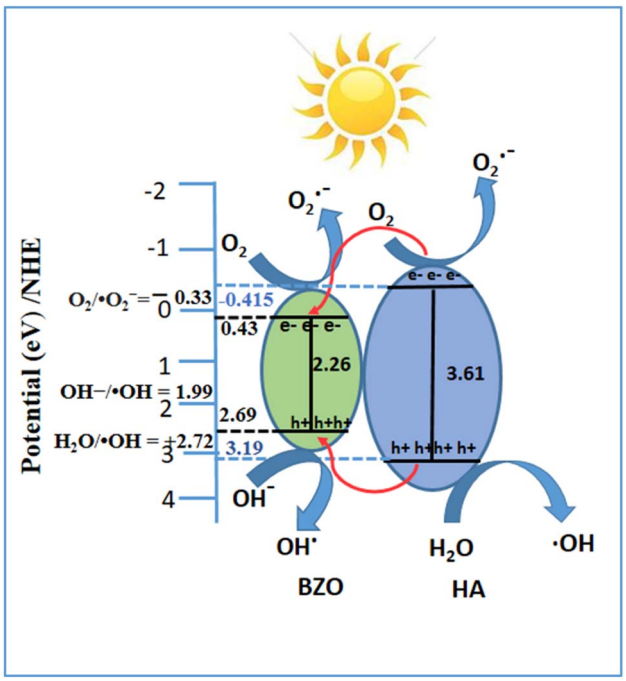

Fig. 11 Schematic band diagram of the BZO-HA composite.

nitrate and dextrose. As presented in Fig. 13, the sensing of the prepared graphite-BZO-HA (10%) electrode for lead nitrate in 0.1 M KCl electrolyte was confirmed by the presence of a redox potential peak at −0.24 V (Fig. 13a) and for dextrose at 0.18 and −0.58 V (Fig. 13b). The redox peaks appeared at varied potential positions with respect to CV of BZO-HA (10–30%) in the bare electrolyte, which confirmed the sensibility of the electrode for lead.

Strong redox peaks were observed for dextrose as well as for lead nitrate using the prepared graphite-BZO-HA (20%) electrode in the potential range of −1.0 V to +1.0 V. The appearance of redox peaks at varied potential positions of −1.02, −0.38, −0.52 and −0.78 V with respect to the bare electrolyte indicates the sensing capacity for lead nitrate and redox peak potentials at −0.48 and −0.60 V for dextrose, as shown in the Fig. 13c and d, respectively. Similarly, the increased HA concentration in the BZO-HA (30%) composite material shows less sensing property towards lead nitrate and dextrose compared to graphite-BZO-HA (20%). Strong redox peaks for dextrose and lead nitrate were observed for the prepared graphite-BZO-HA (20%) electrode in the potential range of −1.0 V to +1.0 V.

The presence of redox peaks at potential positions of −0.07 and 0.48 V indicates the sensing capacity for lead nitrate and redox peak potentials at 0.09 and 0.69 V for dextrose as shown in Fig. 13e and f, respectively. Hence, the obtained data reveal that the BZO-HA (20%) electrode sensing properties towards lead nitrate and dextrose are better than those of BZO-HA (bare HA, 10% and 30%), which confirms that the synthesized BZO-HA (20%) nanocomposite can be used as a better candidate for the sensor applications.

3.4 Antibacterial activity

The synthesized BZO-HA (20%) was analyzed for antibacterial activity against both Gram-positive and Gram-negative bacteria, *S. aureus* and *S. typhi*, with DMSO as a negative control. The potential activity of the sample is directly proportional to the zone of inhibition, as shown in Fig. 14 and Table 4. Past studies revealed several mechanisms for growth inhibition. The positively charged ions, like Ca^{2+} and Na^+, are drawn to the surface of the bacteria whose cellular membranes have negative charges because they contain phosphate and carboxyl groups.[68] The resultant electrostatic interactions may alter the cellular membrane physically, resulting in cell damage and increasing the penetration of the ions.[69] The positive metal ions from BZO-HA can result in significant quantities of reactive oxygen species that lead to denaturation of the proteins inside the cell, particularly those of the ribosomes. These substances, when present in excess, limit cellular respiration, disrupt lipids and nucleic acids, and also trigger a reaction akin to apoptosis.[70]

The presence of minerals like Na^+ and Ca^{2+} in the as-synthesized BZO-HA gives it antibacterial properties. The antibacterial efficacy of BZO-HA was discovered to increase with concentration. This is explicable by the fact that BZO-HA (400 μg) has the highest concentration of Ca^{2+} and Na^+, and the presence of TCP (tricalcium phosphate) which improves Mg^{2+}

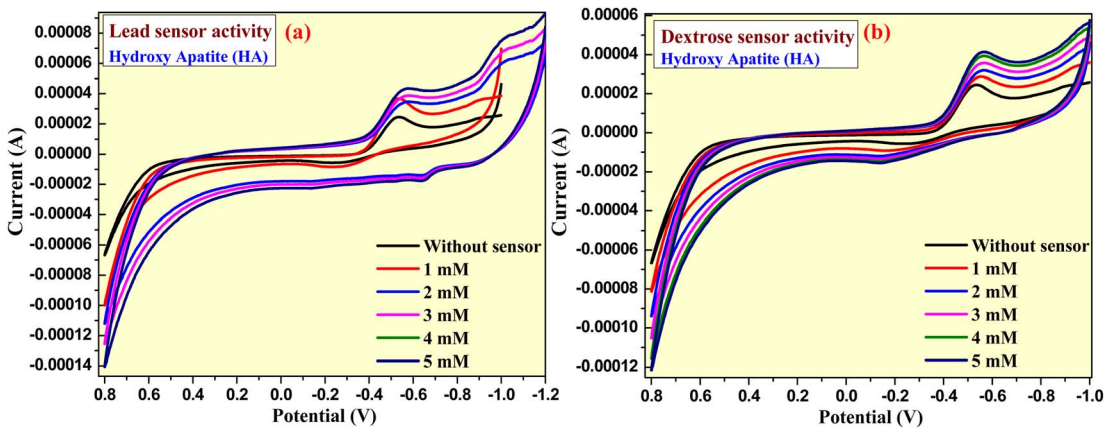

Fig. 12 CV plot of HA electrode for sensing lead nitrate and dextrose molecule at a concentration ranging from 1 to 5 mM (a and b).

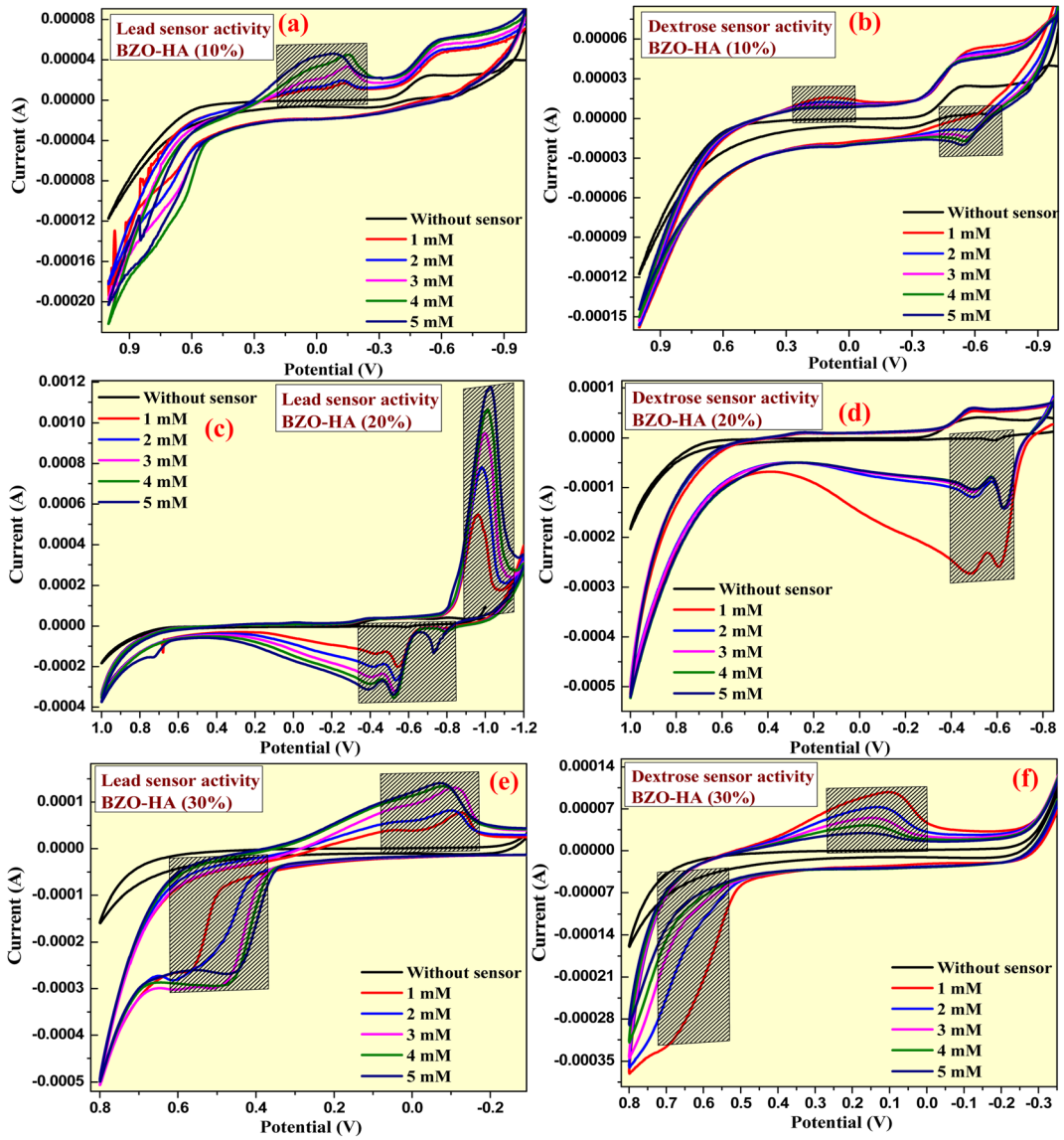

Fig. 13 The CV plots of the prepared BZO-HA electrodes for sensing lead nitrate at concentrations ranging from 1 to 5 mM (a, c and e); and CV plot of the prepared BZO-HA electrodes for sensing dextrose at concentrations ranging from 1 to 5 mM (b, d and f).

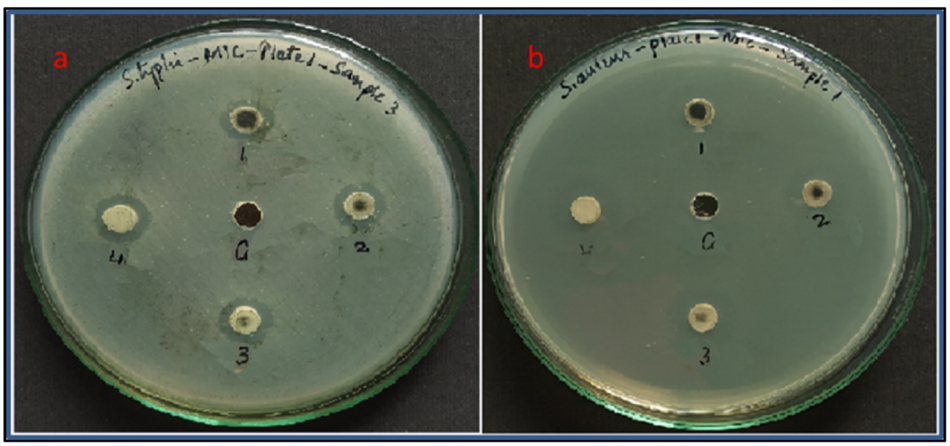

Fig. 14 Inhibition zones of (a) *S. typhi* (b) *S. aureus* for the BZO-HA (20%) sample with concentrations of 1. 100 μg, 2. 200 μg, 3. 300 μg, 4. 400 μg, and C. control.

Table 4 Inhibition zones in mm for BZO-HA (20%) against *S. typhi* and *S. aureus*

Concentrations ($\mu g\ mL^{-1}$)	BZO-HA (20%)	
	S. typhi	*S. aureus*
100	19	15
200	21	18
300	24	20
400	26	23
Control	—	—

and Na^+ solubility and bioresorbability and so enhances the antibacterial activity.[71]

4 Conclusion

In the present work, BZO-HA composites were successfully synthesized by a simple combustion method and SEM-EDS, FTIR, XRD, electrochemical, and UV-vis techniques were employed to characterize the composites. The catalyst efficiency was assessed in the presence of sunlight for degradation of MB and RB dyes under optimum conditions. The BZO-HA (20%) catalyst was proved to be the most efficient one as compared to the other as-prepared photocatalysts. The photogenerated holes, hydroxyl radical, and superoxide anion are responsible for the excellent photocatalytic degradation of MB and RB dyes. In addition, the as-prepared BZO-HA (20%) composite exhibited better antibacterial activity against *S. aureus* and *S. typhi* bacterial pathogens owing to the synergistic effect between BZO and HA particles, and the generation of reactive oxygen species. Moreover, the BZO-HA (20%) composite-modified electrode showed high selectivity for the determination of dextrose and lead nitrate in 0.1 M KCl as an electrolyte over the applied potential range from −0.8 V to +1.0 V for 1–5 mM concentrations of analytes. Finally, these results may be a promising route to prepare new semiconductor-based photocatalysts for a wide spectrum of applications.

Author contributions

K. Pompapathi: experimental work; K. S. Anantharaju: conceptualization and supervision, Arpita Paul Chowdhury: formal analysis and writing the original draft; B. S. Surendra: data acqusition and analysis; B Uma and S Meena: contributed towards data curation and formal analysis; H. C. Ananda Murthy: writing, reviewing and editing.

Conflicts of interest

The authors declare that they have no known competing financial interests or personal relationships that could have appeared to influence the work reported in this paper.

Acknowledgements

The authors are thankful to the Principal and Management for lab facilities and infrastructure.

References

1 N. Baig, I. Kammakakam and W. Falath, *Mater. Adv.*, 2021, **2**, 1821–1871.
2 R. M. Gunnagol and M. H. K. Rabinal, *ChemistrySelect*, 2019, **4**, 6167–6176.
3 F. A. Alharthi, A. Ali Alghamdi, H. S. Alanazi, A. A. Alsyahi and N. Ahmad, *Catalysts*, 2020, **10**, 1457.
4 S. Sabbahi, L. Ben Ayed and A. Boudabbous, *J. Water Health*, 2013, **11**, 590–599.
5 J. Pandey, V. Shrivastava and R. Nagarajan, *Inorg. Chem.*, 2018, **57**, 13667–13678.
6 S. Bhattar, A. Krishnakumar, S. Kanitkar, A. Abedin, D. Shekhawat, D. J. Haynes and J. J. Spivey, *Ind. Eng. Chem. Res.*, 2019, **58**, 19386–19396.
7 D. Wu, T. He, J. Xia and Y. Tan, *Mater. Lett.*, 2015, **156**, 195–197.
8 X. Liu, L. Huang, X. Wu, Z. Wang, G. Dong, C. Wang, Y. Liu and L. Wang, *Chemosphere*, 2018, **210**, 424–432.
9 Y. Luo, L. Cao, L. Feng, J. Huang, L. Yang, C. Yao and Y. Cheng, *J. Mater. Sci. Eng. B*, 2019, **240**, 133–139.
10 A. S. Rajashekharaiah, G. P. Darshan, H. B. Premkumar, P. Lalitha, S. C. Sharma and H. Nagabhushana, *Mater. Chem. Phys.*, 2020, **242**, 122468.
11 L. Wang, C. Hu and L. Shao, *Int. J. Nanomed.*, 2017, **12**, 1227–1249.
12 C. Liao, Y. Li and S. Tjong, *Int. J. Mol. Sci.*, 2019, **20**, 449.
13 S. Christidi, A. Chrysostomou, A. Economou, C. Kokkinos, P. R. Fielden, S. J. Baldock and N. J. Goddard, *Sensors*, 2019, **19**, 4809.
14 S. Nasrazadani and S. Hassani, in *Handbook of Materials Failure Analysis with Case Studies from the Oil and Gas Industry*, Elsevier, 2016, pp. 39–54.
15 N. J. Miller-Ihli, Chapter 13 - Chromium, in *Techniques and Instrumentation in Analytical Chemistry*, ed. M. Stoeppler, Elsevier, 1992, pp. 373–404.
16 L. Minc, in *Encyclopedia of Archaeology*, Elsevier, 2008, pp. 1669–1683.
17 K. M. Pitts and S. W. Lewis, in *Reference Module in Chemistry, Molecular Sciences and Chemical Engineering*, Elsevier, 2018.
18 Z. Qu, Z. Jing, X. Chen, Z. Wang, H. Ren and L. Huang, *J. Environ. Sci.*, 2023, **125**, 349–361.
19 X. He, T. Kai and P. Ding, *Environ. Chem. Lett.*, 2021, **19**, 4563–4601.
20 B. Liu, X. Han, Y. Wang, X. Fan, Z. Wang, J. Zhang and H. Shi, *J. Mater. Sci.: Mater. Electron.*, 2018, **29**, 14300–14310.
21 S. Das Lala, E. Barua, P. Deb and A. B. Deoghare, *Mater. Today Commun.*, 2021, **27**, 102443.
22 B. Nayak and P. K. Misra, *Mater. Chem. Phys.*, 2019, **230**, 187–196.
23 G. Bharath and N. Ponpandian, *RSC Adv.*, 2015, **5**, 84685–84693.
24 C. Shi, C. Lv, L. Wu and X. Hou, *J. Hazard. Mater.*, 2017, **338**, 241–249.
25 P. Hou, C. Shi, L. Wu and X. Hou, *Microchem. J.*, 2016, **128**, 218–225.

26 K. Sharma, S. Sharma, V. Sharma, P. K. Mishra, A. Ekielski, V. Sharma and V. Kumar, *Nanomaterials*, 2021, **11**, 1403.
27 S. Pai, M. S. Kini, R. Mythili and R. Selvaraj, *Environ. Res.*, 2022, **210**, 112951.
28 P. Acharya, M. Kupendra, A. Fasim, K. S. Anantharaju, N. Kottam, V. K. Murthy and S. S. More, *Biotechnol. Lett.*, 2022, **44**, 1175–1188.
29 C. Anupama, A. Kaphle, Udayabhanu and G. Nagaraju, *J. Mater. Sci.: Mater. Electron.*, 2018, **29**, 4238–4249.
30 B. Uma, K. S. Anantharaju, B. S. Surendra, K. Gurushantha, S. S. More, S. Meena, B. Hemavathi and H. C. A. Murthy, *ACS Omega*, 2023, **8**, 9947–9961.
31 V. Jayaraman, C. Ayappan, B. Palanivel and A. Mani, *RSC Adv.*, 2020, **10**, 8880–8894.
32 A. S. Rajashekharaiah, G. P. Darshan, R. B. Basavaraj, Y. V. Naik, D. Kavyashree, S. C. Sharma and H. Nagabhushana, *Opt. Mater.*, 2019, **95**, 109237.
33 J. Pandey, V. Shrivastava and R. Nagarajan, *Inorg. Chem.*, 2018, **57**, 13667–13678.
34 L. Chen, S. Al-Bayatee, Z. Khurshid, A. Shavandi, P. Brunton and J. Ratnayake, *Materials*, 2021, **14**, 4865.
35 M. Fuentes-Pérez, M. Sotelo-Lerma, J. L. Fuentes-Ríos, E. G. Morales-Espinoza, M. Serrano and M. E. Nicho, *J. Mater. Sci.: Mater. Electron.*, 2021, **32**, 16786–16799.
36 V. S. Bystrov, C. Piccirillo, D. M. Tobaldi, P. M. L. Castro, J. Coutinho, S. Kopyl and R. C. Pullar, *Appl. Catal., B*, 2016, **196**, 100–107.
37 S. Sha, L. Zhang, H. Liu, J. Chen, Y. Che, F. Zhang and C. Song, *RSC Adv.*, 2021, **11**, 15598–15607.
38 H. Guo, B. Devakumar, R. Vijayakumar, P. Du and X. Huang, *RSC Adv.*, 2018, **8**, 33403–33413.
39 A. P. Chowdhury, K. S. Anantharaju, S. S. Umare and S. S. Dhar, *Colloids Surf., A*, 2022, **652**, 129841.
40 S. Saber-Samandari, S. Saber-Samandari, M. Gazi, F. Ç. Cebeci and E. Talasaz, *J. Macromol. Sci., Part A*, 2013, **50**, 1133–1141.
41 C. de C. A. Lopes, P. H. J. O. Limirio, V. R. Novais and P. Dechichi, *Appl. Spectrosc. Rev.*, 2018, **53**, 747–769.
42 B. S. Surendra, H. P. Nagaswarupa, M. U. Hemashree and J. Khanum, *Chem. Phys. Lett.*, 2020, **739**, 136980.
43 S. S. Hegde, B. S. Surendra, V. Talapatadur, P. Murahari and K. Ramesh, *Chem. Phys. Lett.*, 2020, **754**, 137665.
44 M. Swamy M, B. S. Surendra, C. Mallikarjunaswamy, S. Pramila and N. D. Rekha, *Environ. Nanotechnol., Monit. Manage.*, 2021, **15**, 100442.
45 S. Meena, K. S. Anantharaju, S. Malini, A. Dey, L. Renuka, S. C. Prashantha and Y. S. Vidya, *Ceram. Int.*, 2021, **47**, 14723–14740.
46 B. S. Surendra, K. Gurushantha, K. S. Anantharaju, M. Rudresh, N. Basavaraju, N. Raghavendra, A. A. Jahagirdar, H. M. Somashekar and H. C. A. Murthy, *New J. Chem.*, 2023, **47**, 3978–3992.
47 B. S. Surendra, T. Kiran, M. V. Chethana, H. S. Savitha and M. S. Paramesh, *J. Mater. Sci.: Mater. Electron.*, 2021, **32**, 25234–25246.
48 N. Raghavendra, H. P. Nagaswarupa, T. R. S. Shekhar, M. Mylarappa, B. S. Surendra, S. C. Prashantha, C. R. Ravikumar, M. R. A. Kumar and N. Basavaraju, *Appl. Surf. Sci. Adv.*, 2021, **5**, 100103.
49 K. Mao, Y. Zhu, J. Rong, F. Qiu, H. Chen, J. Xu, D. Yang, T. Zhang and L. Zhong, *Colloids Surf., A*, 2021, **611**, 125888.
50 G. Meenakshi, B. C. Manjunath, S. C. Prashantha, T. Prashanth and B. S. Surendra, *Sens. Int.*, 2023, **4**, 100237.
51 K. Gurushantha, K. S. Anantharaju, N. Kottam, K. Keshavamurthy, C. R. Ravikumar, B. S. Surendra, A. Murugan and H. C. A. Murthy, *Adsorpt. Sci. Technol.*, 2022, **2022**, 1–13.
52 M. Dinamani, B. S. Surendra, H. C. Ananda Murthy, N. Basavaraju and V. V. Shanbhag, *Environ. Nanotechnol., Monit. Manage.*, 2023, **20**, 100822.
53 B. Wang, P. Li, C. Du, Y. Wang, D. Gao, S. Li, L. Zhang and F. Wen, *RSC Adv.*, 2019, **9**, 41977–41983.
54 P. Govindasamy, B. Kandasamy, P. Thangavelu, S. Barathi, M. Thandavarayan, M. Shkir and J. Lee, *Sci. Rep.*, 2022, **12**, 11572.
55 Y. Deng, M. Xu, X. Jiang, J. Wang, P.-L. Tremblay and T. Zhang, *Environ. Res.*, 2023, **216**, 114808.
56 T. Liu, F. Yang, L. Wang, L. Pei, Y. Hu, R. Li, K. Hou and T. Ren, *Toxics*, 2022, **10**, 555.
57 Z. Mengting, T. A. Kurniawan, S. Fei, T. Ouyang, M. H. D. Othman, M. Rezakazemi and S. Shirazian, *Environ. Pollut.*, 2019, **255**, 113182.
58 D. R. Paul, S. Gautam, P. Panchal, S. P. Nehra, P. Choudhary and A. Sharma, *ACS Omega*, 2020, **5**, 3828–3838.
59 T. A. Dontsova, A. S. Kutuzova, K. O. Bila, S. O. Kyrii, I. V. Kosogina and D. O. Nechyporuk, *J. Nanomater.*, 2020, **2020**, 1–13.
60 C. Mardani, M. Y. Rizal, R. Saleh, A. Taufik and S. Yin, *Appl. Surf. Sci.*, 2020, **530**, 147297.
61 A. Krishnan, P. V. Vishwanathan, A. C. Mohan, R. Panchami, S. Viswanath and A. V. Krishnan, *Surf. Interfaces*, 2021, **22**, 100808.
62 E. Kamaraj, S. Somasundaram, K. Balasubramani, M. P. Eswaran, R. Muthuramalingam and S. Park, *Appl. Surf. Sci.*, 2018, **433**, 206–212.
63 G. Murugadoss, D. D. Kumar, M. R. Kumar, N. Venkatesh and P. Sakthivel, *Sci. Rep.*, 2021, **11**, 1080.
64 S. S. Singh, A. Kumar, N. Kataria, S. Kumar and P. Kumar, *J. Environ. Chem. Eng.*, 2021, **9**, 106266.
65 C. Sudhakar, R. Devi, S. Nikhil, P. Kalyani, A. Suganthi and M. Rajarajan, *Orient. J. Chem.*, 2022, **38**, 144–150.
66 S. Chahal, N. Rani, A. Kumar and P. Kumar, *Vacuum*, 2020, **172**, 109075.
67 A. Khatri and P. S. Rana, *Phys. B*, 2020, **579**, 411905.
68 M. Wang, M. Li, Y. Wang, Y. Shao, Y. Zhu and S. Yang, *J. Mater. Chem. B*, 2021, **9**, 3401–3411.
69 D. Predoi, S. Iconaru, M. Predoi, M. Motelica-Heino, R. Guegan and N. Buton, *Nanomaterials*, 2019, **9**, 515.
70 V. Sanyal and C. R. Raja, *Appl. Phys. A*, 2016, **122**, 132.
71 P. Phatai, C. M. Futalan, S. Kamonwannasit and P. Khemthong, *J. Sol-Gel Sci. Technol.*, 2019, **89**, 764–775.